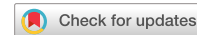


# communications

## earth & environment

### ARTICLE



<https://doi.org/10.1038/s43247-024-01214-z>

OPEN

## Large igneous province activity drives oceanic anoxic event 2 environmental change across eastern Asia

R. Takashima<sup>1</sup>✉, D. Selby<sup>2</sup>, T. Yamanaka<sup>3</sup>, Y. Kuwahara<sup>4</sup>, H. Nakamura<sup>5</sup>, K. Sawada<sup>6</sup>, M. A. Ikeda<sup>7</sup>, T. Ando<sup>8</sup>, K. Hayashi<sup>9</sup>, M. Nishida<sup>8</sup>, T. Usami<sup>9</sup>, D. Kameyama<sup>8</sup>, H. Nishi<sup>10</sup>, A. Kuroyanagi<sup>11</sup> & B. R. Gyawali<sup>12</sup>

During mid-Cretaceous Oceanic Anoxic Event 2, significant increase of atmospheric carbon dioxide concentrations from the eruption of the large igneous provinces is hypothesized to have induced a humid climate and an elevation in nutrient runoff from continents to the oceans, resulting in oxygen depletion in the ocean. However, hitherto there is limited insight into the driving factors of Oceanic Anoxic Event 2 from the Pacific and Asian continental margins, even though the former and the latter were the largest ocean and landmass at that time. Here, a multiproxy analysis for the Oceanic Anoxic Event 2 interval of the Yezo Group –deposited on northwestern Pacific along the active Asian continental margin– is interpreted to identify seven volcanic pulses, five of which may have elevated humidity, weathering intensity, and vegetational change in the eastern margin of Asia. Moreover, oxygen depletion occurred simultaneously in the northwest Pacific. Given that these environmental changes in the eastern margin of Asia were penecontemporaneous with the global carbon burial intervals during Oceanic Anoxic Event 2, the elevated nutrient supply from the Asian continental margin to the Pacific Ocean may have, in part, contributed to the worldwide depletion of oxygen of the ocean during Oceanic Anoxic Event 2.

<sup>1</sup> Tohoku University Museum, Tohoku University, Aramaki Aza Aoba 6-3, Aoba-ku, 980-8578 Sendai, Miyagi, Japan. <sup>2</sup> Department of Earth Sciences, Durham University, DH13LE Durham, UK. <sup>3</sup> School of Marine Resources and Environment, Tokyo University of Marine Science and Technology, 4-5-7 Konan Minato-ku, Tokyo 108-8477, Japan. <sup>4</sup> Department of Environmental Changes, Faculty of Social and Cultural Studies, Kyushu University, Motoooka, Fukuoka 819-0395, Japan. <sup>5</sup> Department of Earth and Planetary Sciences, Faculty of Science, Hokkaido University, N10W8, Sapporo 060-0810, Japan. <sup>6</sup> Graduate School of International Resource Sciences, Akita University, 1-1 Tegatagakuen-machi, Akita 010-8502, Japan. <sup>7</sup> Research Institute of Energy, Environment and Geology, Industrial Technology and Environment Research Department, Hokkaido Research Organization, Nishi-12, Kita-19, Kita-ku, Sapporo, Hokkaido 060-0819, Japan. <sup>8</sup> Department of Earth Science, Graduate School of Science, Tohoku University, Aramaki Aza Aoba 6-3, Aoba-ku, Sendai 980-8578, Japan. <sup>9</sup> 2ndLabo, Inc., Nishi-shinjuku 2-4-1, Shinkuju-ku, Tokyo 163-0806, Japan. <sup>10</sup> Institute of Dinosaur Research, Fukui Prefectural University, Matsuoka kenjojima 4-1-1, Yoshida-gun Eiheijicho, Fukui 910-1142, Japan. <sup>11</sup> Department of Geology, Tri-Chandra Campus, Tribhuvan University, Kathmandu, Nepal. <sup>12</sup> Lumbini Engineering Management and Science College, Pokhara University, Pokhara, Nepal. ✉email: [reishi.takashima.a7@tohoku.ac.jp](mailto:reishi.takashima.a7@tohoku.ac.jp)

Oceanic Anoxic Event 2 (OAE2) occurred between 94.5 and 93.9 million years ago and was caused by rapid warming due to the massive release of  $\text{CO}_2$  associated with the eruption of the large igneous provinces (LIPs)<sup>1</sup>. The expansion of anoxic environments and acidification and eutrophication of the global surface ocean during OAE2 led to the significant faunal turnover of marine microbiota<sup>2</sup>. The features of OAE2, for example, a decline in dissolved oxygen in the global ocean because of increased seawater temperature, atmospheric  $\text{CO}_2$  levels, and nutrient inputs to the ocean have also been observed as one of the most recent state-of-changes in Earth's history since the 1950s<sup>3</sup>. Therefore, OAE2 has long been studied extensively to predict future climatic and environmental changes to our current warming Earth. Various techniques have been used to investigate the evidence for global warming during the Cretaceous period and the underlying mechanisms responsible for the resulting environmental changes and ecosystem impacts. Consequently, our understanding of OAE2 has significantly improved over the past few decades. However, certain issues remain unresolved.

First, although there is little doubt that LIPs are associated with the onset and persistence of OAE2, various LIPs, such as the Caribbean LIP, High Arctic LIP, Madagascar Flood Basalt, and 2nd Ontong Java Plateau have been found to have erupted during the temporal framework of OAE2 (Fig. 1A); it has not been determined, which LIP or LIPs caused the environmental change and to what extent<sup>4,5</sup>. Second, OAE2 is marked by a cooling and re-oxygenation interval known as the "Plenus Cold Event (PCE)"<sup>6</sup>. Additionally, there is disagreement about whether this cooling is attributable to a decrease in igneous activity or an increase in organic carbon burial<sup>5,7</sup>. Third, continental weathering may have affected the persistence or cessation of OAE2 and raised the high temperatures after OAE2 despite the demise of LIP activity. However, it is unclear whether the continental crust or basalt weathering was more influential<sup>5,8,9</sup> or both. Fourth, the impact of OAE2 on terrestrial fauna and flora remains poorly demonstrated, except for SE France<sup>10</sup>.

Furthermore, our understanding of the impact of OAE2 on the Pacific Ocean is limited compared to the Tethys Sea and the Atlantic Ocean. Recently, it has been shown that the continental margin of the Pacific maintained relatively oxic conditions during

OAE2<sup>11,12</sup>. Although the Pacific Ocean was the largest ocean during the Cretaceous and the locus of the major LIPs, such as the Caribbean LIP and Ontong Java Plateau, its influence on the global carbon cycle and climate during OAE2 remains poorly understood.

The Yezo Group, which is exposed in northern Japan, was deposited approximately at 45° N along the Asian active continental margin in the northwestern Pacific Ocean (Fig. 1A). The Saku Formation of the Yezo Group, which is exposed in the Omagarizawa Creek (OC) section, contains a 445-m-thick interval of OAE2 in short-definition and a 590-m-thick interval in long-definition (Fig. 2)<sup>13</sup>, which may be one of the thickest OAE2 strata in the world. The OAE2 of the OC section mainly comprises mudstone with intercalated turbidite sandstones. The Yezo Group is significant because the mudstone contains abundant terrigenous detritus and marine macro and microfossils<sup>11,14</sup>. Therefore, it is essential to understand not only the marine environment of the northwestern Pacific Ocean but also the terrestrial floral and climatic changes in its hinterland of the eastern Asian continent.

Additionally, numerical modeling of the Cretaceous climate demonstrated that the basin of the Yezo Group and its hinterland were located in areas associated with the highest precipitation levels during elevated levels of  $p\text{CO}_2$  (Fig. 1B)<sup>15</sup>. Considering extremely high-sedimentation rates of the strata in the OC section, multiproxy analyses, such as initial osmium-isotope compositions ( $^{187}\text{Os}/^{188}\text{Os}$ – $\text{Os}_i$ ) and carbon isotopes, clay mineral crystallinity, and organic- and inorganic geochemistry of the Yezo Group in the OAE2 interval, can resolve the previously mentioned problems and the land-ocean relationships to LIP activities in the northwestern Pacific Ocean.

## Results and discussion

**Stratigraphy of OAE2 in the Yezo Group.** The analyzed interval in the OC section is composed mainly of three lithological units. The lower unit (0–220 m level) is mainly mudstone with occasional intercalation of thin-bedded (1–5 cm thick) turbidites. The middle unit (220–310 m level) is characterized by frequent intercalation of thick-bedded (10–30 cm thick) turbidite sandstones. The upper unit is mostly dark gray mudstone with

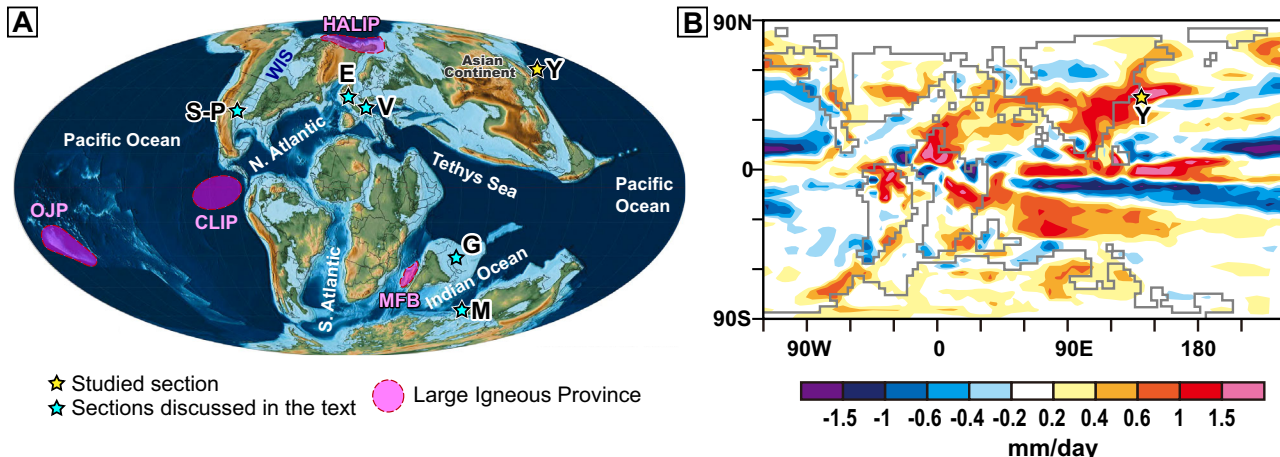


**Fig. 1 Paleogeographic and precipitation maps during Late Cenomanian.** **A** Late Cenomanian palaeogeographic map<sup>43</sup> illustrating studied section, locations of Large Igneous Province and sections of OAE2 sequence discussed in the text. Locations: Y – Yezo Group, Hokkaido (Japan); S-P – SH#1 and Portland cores, Colorado (USA) (WIS – Western Interior Seaway); E – Eastbourne (UK); V – Vocontian Basin (SE France); G – Gongzha section (southern Tibet, China); M – Mentelle Basin (SE of Australia). The Ontong Java Plateau, Madagascar Flood Basalt and High Arctic and Caribbean Large Igneous Provinces are marked on the map as OJP, MFB, HALIP and CLIP, respectively. **B** Map showing change in mean annual precipitation (mm/day) when  $p\text{CO}_2$  is ten times pre-industrial level<sup>15</sup>.

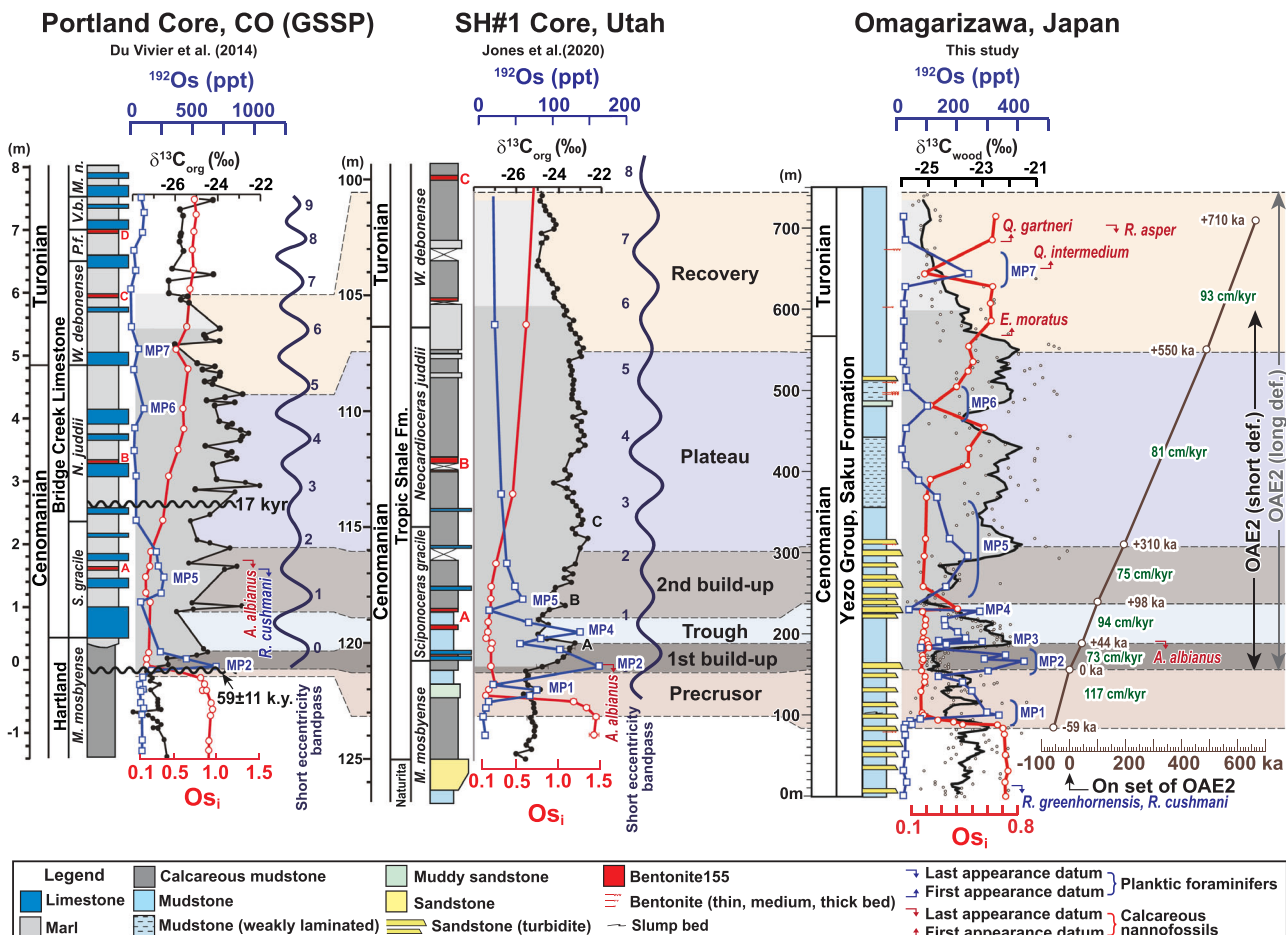


**Fig. 2 Chemo- and biostratigraphic correlation of OAE2 interval.** A chemostratigraphic correlation ( $\delta^{13}\text{C}_{\text{org}}$ ,  $^{192}\text{Os}$ ,  $\text{Os}_i$ ) of three OAE2 interval sites of Portland core<sup>21</sup>, Colorado, SH#1 core<sup>13</sup>, Utah, USA, and Omagarizawa Creek, Hokkaido, Japan. The five segments, named the first build-up, trough, second build-up, plateau, and recovery, are divided based on  $\delta^{13}\text{C}$  curve proposed by ref. <sup>18</sup>.

sporadic intercalation of thin turbidite sandstones. Although the occurrences of the age-diagnostic microfossils are quite sporadic in the sequence under study, several important index species of planktic foraminifera and calcareous nannofossils have been identified (Fig. 2). In addition to the biostratigraphy, carbon and osmium isotope stratigraphy allows a detailed correlation between the representative OAE2 reference sequences (SH#1 and Portland cores) of the Western Interior Basin (WIB)<sup>7,13,16,17</sup> and the Saku Formation in the OC section (Figs. 1A, 2). Here, we have divided the  $\delta^{13}\text{C}$  curve of the OAE2 interval into five segments, as shown for the Eastbourne section<sup>18</sup> (Fig. 1A): The five segments are named the first build-up, trough, second build-up, plateau, and recovery (Fig. 2). The base of first build-up segment is important because it defines the onset of OAE2. The first build-up segment at Eastbourne section, defined by ref. 18, shows a large positive shift in the overall trend of  $\delta^{13}\text{C}$ , but it is accompanied with a few minor positive peaks in its lower part. Therefore, in our studied section, we place the base of first build-up segment at the 155 m level where the overall positive trend starts, although the prominent positive excursion occurs between 175 and 188 m (Fig. 2). We further have referred to an interval of the  $\delta^{13}\text{C}$  curve ranging from the onset of non-radiogenic osmium isotopic values to the first build-up as the “Precursor” segment. This segment is characterized by two sets of minor negative and positive peaks in  $\delta^{13}\text{C}$  profile.

Based on the detailed stratigraphic correlation between the OC section and cores of WIB, the OAE2 interval in short-definition<sup>13</sup>

in the OC section is measured to be 445 m thick, making it one of the thickest known OAE2 intervals (Fig. 2). With no known hiatus, the sedimentation rate of OAE2 in the OC section is estimated to be as high as 73–117 cm/kyr. The upper PCE interval (second build-up segment), which corresponds roughly to a 220–320 m interval, frequently shows intercalation of thicker turbidite sandstones. This intercalation of thicker turbidites and/or channel conglomerates in the upper PCE interval are also demonstrated at other sections in the Yezo Group<sup>11,19</sup>, indicating a possible eustatic sea-level fall and basin-ward migration of submarine fans, and propagation of incised valleys. Although local tectonic uplift around the Yezo basin during this period cannot be ruled out, a contemporaneous sea-level fall has also been reported from Mexico<sup>20</sup> and WIB<sup>17</sup>.

**Magmatic activity around Oceanic Anoxic Event 2.** The temporal relationship between magmatism during the OAE2 period has been extensively evaluated utilizing Os<sub>i</sub> stratigraphic profiles<sup>1,5,7,13,21–23</sup>. Our study of the OAE2 interval in the OC section is consistent with other sections, in that it shows a shift to nonradiogenic Os<sub>i</sub> before the onset of OAE2, followed by similar values up to the late phase of OAE2 (the Precursor to the lower part of the Plateau segment). This is then followed by a gradual increase to more radiogenic Os<sub>i</sub> values toward the end of OAE2 (upper Plateau to Recovery segment). However, our high-resolution Os<sub>i</sub> profile reveals four short-lived minor increases in

$Os_i$  (at the 140–150, 180–190, 210–230, and 240–260 m levels), suggesting a quiescence in magmatic activity and/or an increase in continental weathering. In addition, we found two brief but prominent trends to lower  $Os_i$  (at the 460–480 and 630–680 m levels) through the stratigraphic interval, recording a gradual increase in  $Os_i$  in the latter phase of OAE2 (Fig. 3). Similar trends are also identified from the International Ocean Discovery Program (IODP) Site U1516 core recovered from the Mentelle Basin in eastern Indian Ocean<sup>23</sup> (Fig. 1A), indicating magmatic activities during the latter phase of OAE2. Although the magnitudes of decrease are not prominent, the Portland core also shows slightly lower  $Os_i$  at the same horizons (Fig. 2).

The common osmium abundance (presented as  $^{192}\text{Os}$ ) has been used as a proxy for magmatic activity across the OAE2 interval<sup>5,7,23–25</sup>. The  $Os_i$  values and  $^{192}\text{Os}$  contents in the OC section are negatively correlated, and  $^{192}\text{Os}$  contents, as with previous OAE2 sections, are inferred to detect fluctuations in magmatic activity. To eliminate differences in the sedimentation rate, we also present  $^{192}\text{Os}/\text{Al}$  (Fig. 3) since the studied sequence is mainly controlled by terrigenous input. The  $^{192}\text{Os}$  and  $^{192}\text{Os}/\text{Al}$  data indicate seven pulses of magmatic activity (MP1–7) that

are punctuated by an increase in  $^{192}\text{Os}/\text{Al}$  and a decrease in  $Os_i$  (Fig. 3). Since  $^{192}\text{Os}$  abundance ranges typically between 10 and 30 ppt in the upper Cenomanian to lower Turonian in the Yezo Group<sup>21</sup>, intervals of a magmatic pulse corresponding to OAE2 are characterized by high  $^{192}\text{Os}$  abundance (>100 ppt; Fig. 2).

This study identifies seven magmatic pulses (MP1–7) associated with the OAE2 interval. The first magmatic pulse (MP1) is found just above the initial shift to non-radiogenic  $Os_i$ , before the onset of OAE2. The same pulse is also found in the SH#1 core and is considered to indicate the first igneous activity just prior to the onset of OAE2 (Fig. 2). The second pulse (MP2) occurs in the first build-up segment and is characterized by the highest value in  $^{192}\text{Os}/\text{Al}$  and  $^{192}\text{Os}$ , indicating the largest magmatic activity of the OAE2 interval. The corresponding pulse was observed in Portland<sup>21</sup> and SH# cores<sup>13</sup> (Fig. 2) as well as the Tibetan Tethys sediment at Gongzha section (Fig. 1A)<sup>23</sup>, showing the highest  $^{192}\text{Os}$  contents in their sequence in former two cores. The MP3 and MP4 are very short-lived peaks and are contained in the trough segment. Although the MP3 was not detected in the Portland and SH#1 cores due to lower sample resolution, the

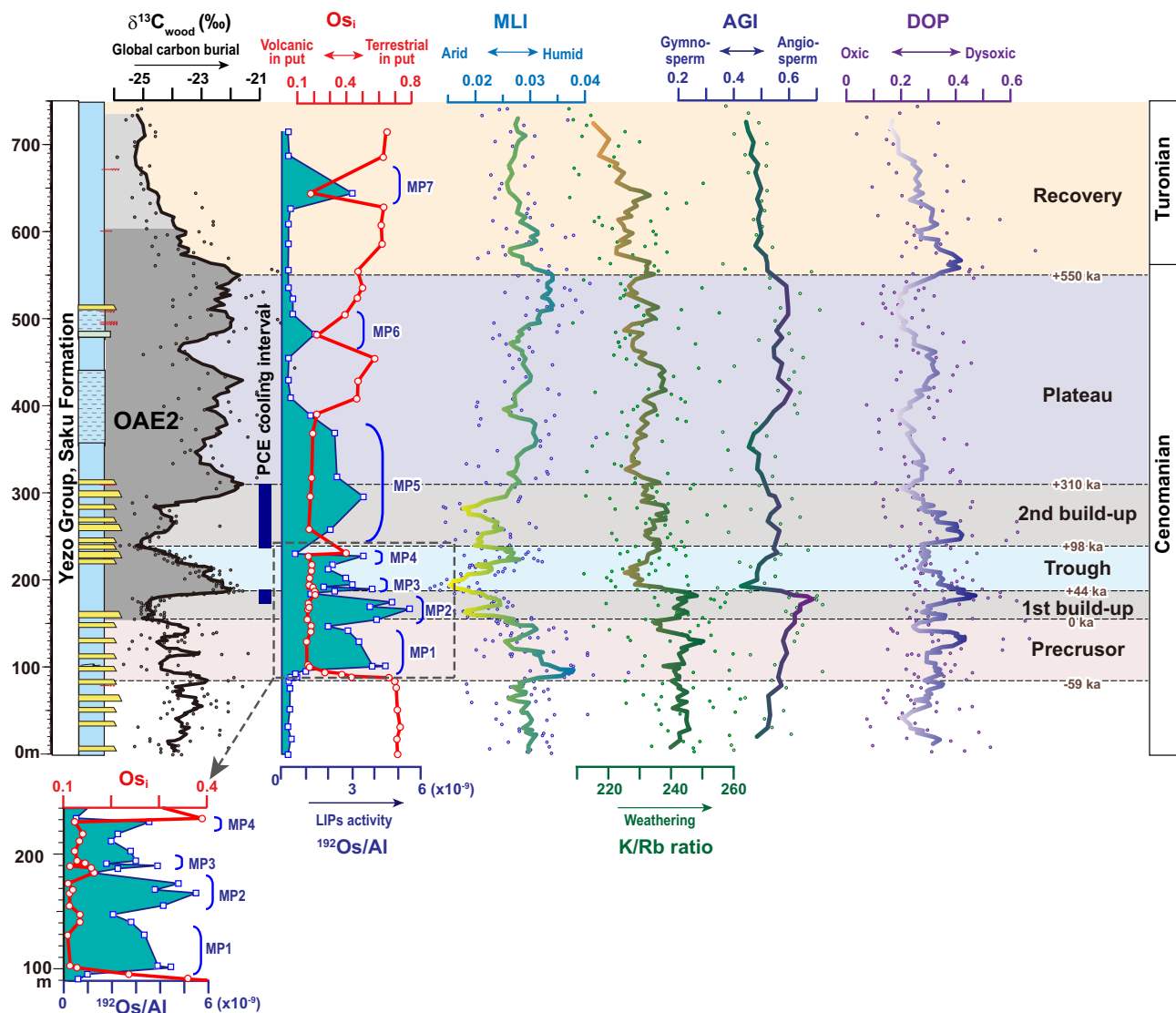


**Fig. 3 Multi-proxy analysis of OAE2 in the studied sequence.** Litho- and chemostratigraphical and geochemical data of the OAE2 interval of the studied sequence.  $Os_i$ : initial  $^{187}\text{Os}/^{188}\text{Os}$  compositions. MLI Modified Lanson index of the illite crystallinity index proposed by ref. <sup>26</sup>. DOP Degree of pyritization, AGI Angiosperm/gymnosperm index.

MP4 was identified in the SH#1 core (Fig. 2). A brief but distinct increase in  $^{192}\text{Os}/\text{Al}$  was observed just above MP4, suggesting a temporary reduction of igneous activity and/or strengthening of continental weathering.

The fifth pulse (MP5) is marked by a broad peak spanning from the Second build-up to the lower Plateau segment, and a corresponding peak is seen at the Portland and SH#1 cores and the Tibetan Tethys sediment<sup>23</sup>. After this peak, either global continental weathering began to predominate, or magmatism waned based on the gradual increase in  $^{192}\text{Os}/\text{Al}$  after this pulse (Figs. 2, 3).

The MP6 and MP7 are short-lived peaks in the upper Plateau and middle Recovery segments, respectively, coincident with distinct more nonradiogenic  $^{192}\text{Os}/\text{Al}$  (Fig. 3). These two pulses which were also identified from Portland core (Fig. 2) and Mentelle Basin<sup>23</sup> (Fig. 1A) and maybe a global signature, suggests that igneous activity was intermittent during the late stages of OAE2 and may have contributed to the persistence of a warm climate in the latter part of and after OAE2<sup>9</sup>.

Based on the correlation between  $^{192}\text{Os}/\text{Al}$  and cooling episodes of the PCE shown in Fig. 3, the first cooling interval of PCE coincides with a shift to lower  $^{192}\text{Os}/\text{Al}$  and a more positive  $\delta^{13}\text{C}$  between MP2 and MP3. This suggests that decreased magmatic activity and increased global carbon burial may have induced the first cooling phase of PCE<sup>5</sup>. On the other hand, the latter cooling interval of PCE is characterized by a higher  $^{192}\text{Os}/\text{Al}$  of MP5 and a positive excursion of  $\delta^{13}\text{C}$ , indicating that the outgassing of  $\text{CO}_2$  from magmatic activity overwhelmed global carbon burial during the Second build-up segment.

**Changes in precipitation, chemical weathering, and vegetation in the eastern margin of the Asian continent during OAE2.** According to numerical modeling<sup>15</sup>, the hinterland of the Yezo Group (eastern margin of the Asian continent) was characterized by one of the highest precipitation areas during elevated  $p\text{CO}_2$  levels (Fig. 1B). The illite crystallinity index provides a useful indication of the intensity of precipitation or continental moisture<sup>26,27</sup>. Specifically, the modified Lanson index (MLI) has been applied to reconstruct changes in precipitation of the Indian Monsoon during the Last Glacial Maximum on the southern slope of the Central Himalaya<sup>27</sup>. The MLI of the OAE2 interval in the OC section (Fig. 3) is a significant demonstration of the linkage among terrestrial climate, continental runoff, and dissolved oxygen level of the ocean in the Asian continental margin in response to LIP activity and intensity. The MLI's five-point moving average curve shows a significant increase in MLI during MP1, which could indicate an increase in volcanic outgassing of LIPs that led to a humid climate in the eastern margin of Asia, as supported by numerical modeling<sup>15</sup> (Fig. 4A). In contrast, the first build-up, trough, and second build-up segments experienced a relatively arid climate, despite magmatic activities (MP2 and 3). The global expansion of ocean anoxia resulted in the massive burial of organic carbon, leading to a decrease in  $p\text{CO}_2$  that could have contributed to the arid conditions in the eastern Asian continental margin. Despite a relatively arid interval, a significant increase in MLI is observed in the horizons of the latest phases of MP2, MP4, MP5, and MP6, indicating that humidity increased in response to the LIP activity (Fig. 4A). Furthermore, the MLI shows an overall increase throughout the Plateau segment, and it remains relatively high during the Recovery segment (Figs. 3, 4C). This trend is consistent with the continuation of warm and humid conditions during the latter stages and after the OAE2 interval, as previously documented<sup>9,28–30</sup>.

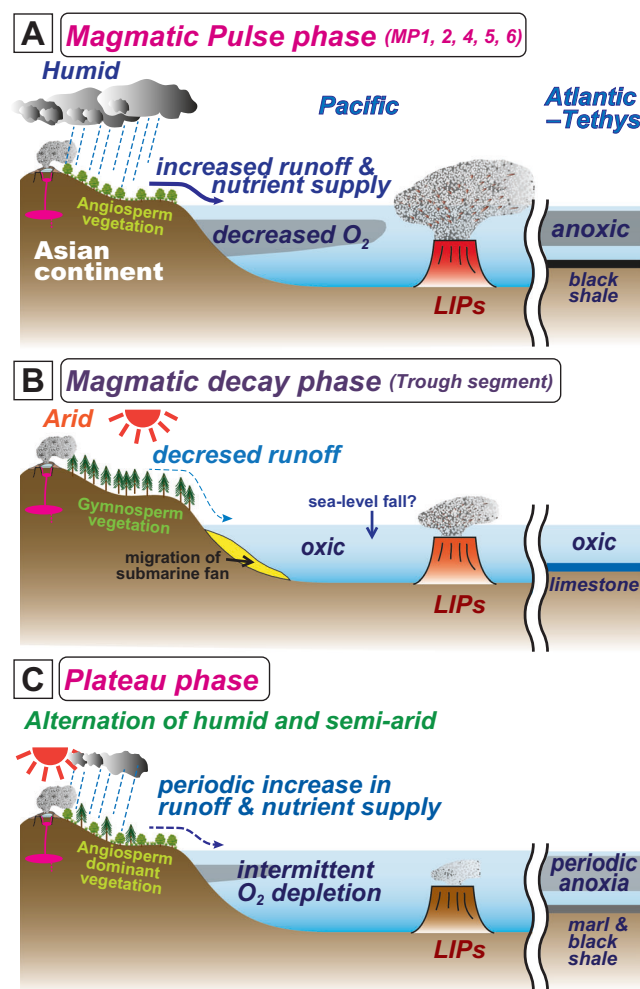


**Fig. 4 Schematic climatic and oceanographic models during OAE2.**

A tentative model for the relationship between LIP activity, climate, oceanographic conditions, and vegetation during OAE2 along the eastern margin of Asia, the Pacific Ocean and Tethys-Atlantic oceans. **A** Model for MP1, 2, 4, 5, 6 in  $^{192}\text{Os}/\text{Al}$  curve (Fig. 3). **B** Model for Trough segment in  $\delta^{13}\text{C}$  curve (Fig. 3). **C** Model for Plateau segment in  $\delta^{13}\text{C}$  (Fig. 3).

Chemical weathering plays a crucial role in OAEs as it controls the supply of nutrients from the land to the ocean and the uptake of  $\text{CO}_2$ . Global chemical weathering fluxes from continental arcs have been shown to dominate over the past 400 Myr<sup>31</sup>. Therefore, it is essential to reconstruct the weathering history of the Yezo Group during OAE2 since it was accumulated along the Asian continental arc. The K/Rb ratio of mudstone is a key proxy for assessing the level of chemical weathering<sup>32</sup>, even though potassium and rubidium have similar ionic radii, potassium has a stronger bonding force than rubidium. Hence, rubidium is more readily leached, with a higher ratio indicating increased progression of chemical weathering of the continental crust. Although there is a slight lag, the increase in K/Rb corresponds with the magmatic pulses, except for MP3. The K/Rb trend also shows a similarity with the angiosperm/gymnosperm index profile. The MLI curve occasionally diverges from the K/Rb trend, especially during the earlier stage of OAE2. This could suggest that chemical weathering during OAE2 may have been influenced by vegetation and  $p\text{CO}_2$ , rather than precipitation, along the Asian continental margin. Additionally, high K/Rb values are observed in the precursor and first build-up segments, whereas the values gradually decrease above the trough segment.

This decline in K/Rb suggests that chemical weathering decreased during the latter phase of OAE2 along the eastern Asian margin. This trend is like the trend observed in  $\delta^7\text{Li}$ , which reflects global silicate weathering intensity<sup>33</sup>. The decline in chemical weathering in the upper part of OAE2 is consistent with the high sea surface temperature that persisted despite the decrease in magmatic activity during the latter part of and after OAE2 (Fig. 4)<sup>9,33</sup>.

Angiosperm/Gymnosperm index (AGI) is calculated as the aromatic triterpenoid/diterpenoid ratio (ar-AGI)<sup>34</sup> rather than aliphatic compounds (AGI)<sup>35</sup> to better represent the source vegetation in the studied samples predominated by aromatic terpenoids. The sudden and rapid increase in diversity and geographic spread of angiosperms occurred in mid-Cretaceous<sup>36–38</sup>, making the AGI of the OC section (Fig. 3) important in understanding the impact of climate change on the evolution of vegetation during OAE2. The proportion of angiosperms increased from the Precursor to the first build-up segment (Fig. 4A). However, gymnosperms rapidly became dominant during the trough segment (Figs. 3 and 4B), followed by increased angiosperms in the Second build-up and the Plateau segment (Fig. 4A, C). However, they returned to the preOAE2 AGI values during the Recovery segment. The tendency of gymnosperm expansion during the cool and dry periods of the first half of the PCE is opposite to that observed in the Vocontian Basin (Fig. 1A), where the gymnosperms flourish during the wet maximum of OAE2. In contrast, to the Vocontian Basin which was in an arid climatic zone during the mid-Cretaceous, the Yezo Group hinterland was in a wet climatic zone<sup>10</sup>. The extremely humid conditions may have caused the expansion of angiosperms or increased the number of aquatic plants among angiosperms. Although there are very few studies on the changes in terrestrial vegetation during OAE2, the limited data illustrate large variations in vegetation both locally and regionally during OAE2, suggesting different regional responses. Interestingly, the AGI in the Yezo Group does not show significant differences before and after OAE2, suggesting that OAE2 itself may not have contributed directly to the expansion of angiosperms, at least in the eastern Asian continental margin.

**Dissolved oxygen in the northwestern Pacific along the Asian continental margin.** The degree of pyritization (DOP) is a useful indicator of the dissolved oxygen levels or redox conditions in the bottom waters. It is calculated as the ratio of iron in pyrite to the total amount of iron in the sediments. The DOP boundary values are <0.45, 0.45–0.75, and >0.75, indicating oxic bottom water conditions, restricted bottom water conditions, and euxinic bottom water conditions, respectively<sup>39</sup>. According to the previous studies on the Yezo Group, the DOP of the OC section suggests that the northwestern Pacific Ocean was largely oxic throughout the OAE2 interval<sup>11</sup>. However, there are four intervals in the section where the oxygen concentration decreased. Notably, two of these intervals coincide with the global carbon burial intervals of the first and second build-up segments (Fig. 4A). These observations indicate that while the northwestern Pacific was largely oxic during OAE2, there were periods of decreasing oxygen concentrations, particularly during the carbon burial intervals.

The first peak of DOP occurs in the same horizon as the MP1 of the Precursor segment. In contrast, this horizon is accompanied by only a minor positive shift in  $\delta^{13}\text{C}$ . Although the  $\delta^{13}\text{C}$  curve at this horizon demonstrates that global carbon burial was insignificant, higher DOP may represent a global oxygen depletion that preceded OAE2 because thallium isotopic ratios ( $\epsilon^{205}\text{Ti}$ ) indicate anoxia on the seafloor had already begun 40,000

years before the onset of OAE2<sup>40</sup>. The timing of the four dysoxia peaks coincides with weathering intensity proposed by elevated K/Rb in the OC section, suggesting that increased nutrient supply from the eastern margin of the Asian continent may have also contributed to the expansion of global ocean anoxia (Fig. 4A). Indeed, numerical modeling studies for OAEs demonstrate that increased nutrient supply from the continents to the oceans is a necessary condition for the expansion of anoxia in the oceans<sup>41,42</sup>. Since eastern Asia was one of the largest land masses during the mid-Cretaceous<sup>43</sup>, increased runoff could have contributed to the significant nutrient export to the ocean and the expansion of global anoxia.

## Methods

**Sampling procedure and microfossil analysis.** Approximately 500 mudstone samples from the Yezo Group were collected at 0.3- to 5-m-stratigraphic intervals. Dry sample aliquots of 400 g were disaggregated using sodium tetraphenylborate plus sodium chloride. The disaggregated sediment was washed over a 64- $\mu\text{m}$  sieve and dried at 50 °C. Foraminiferal specimens (all) and wood fragments (more than 100 fragments per sample) were removed from the processed samples. Nannofossils were viewed using simple smear slide preparations.

**Carbon isotope.** Collected wood fragments were washed in methanol in an ultrasonic bath before immersion in 1 N HCl acid for 24 h. The wood fragments were then dried and crushed to powder. The carbon isotope of the total organic carbon in the acid-treated powdered wood samples was then measured using a mass spectrometer (IsoPrime, GV Instruments) in line with an elemental analyzer (EuroEA3000, EuroVector) at the Tokyo University of Marine Science and Technology. Each sample was run in duplicate. Carbon isotopic ratios were expressed in ‰, relative to the Vienna Pee Dee Belemnite standard. The precision of the  $\delta^{13}\text{C}$  measurements was  $\pm 0.1\text{‰}$ .

**Osmium isotopes.** Fresh, unweathered, vein bereft samples of ~250 g were collected from outcrop of the OC section. From these samples between 30–50 g were cut using a rock saw and polished using a grinding/polishing machine to remove any cut marks and potential metal contamination. Samples were then dried at 50 °C. The samples were powdered (~30  $\mu\text{m}$ ) in ceramic containers using high-purity crushing techniques. The ceramic containers were cleaned using high-purity sand, then washed and finally rinsed with ethanol. The prepared powders were analyzed in the Source Rock and Sulfide Geochronology and Geochemistry Laboratory at Durham University utilizing isotope dilution negative ion mass spectrometry<sup>44</sup>. In brief, sample powders (~1.0 g), together with a known amount of mixed  $^{185}\text{Re} + ^{190}\text{Os}$  tracer solution were digested in sealed Carius tubes with 8 mL of 0.25 g/g  $\text{CrO}_3$  in 4 N  $\text{H}_2\text{SO}_4$  for ~48 h at 220 °C, principally leaching hydrogenous Re and Os (i.e., organic matter). The Os fraction was isolated and purified via chloroform extraction with back reduction into HBr and  $\text{CrO}_3\text{-H}_2\text{SO}_4\text{-HBr}$  microdistillation. The Re fraction was isolated via NaOH-acetone extraction and anion chromatography. Isotopic ratios of samples and solution standards (Re STD and DROSS) were measured in negative mode on a Thermo Triton thermal ionization mass spectrometer (TIMS) in the Arthur Holmes Laboratory at Durham University. Running average values for  $^{187}\text{Os}/^{188}\text{Os}$  and  $^{187}\text{Re}/^{185}\text{Re}$  solution standards to the time of these analyses (6/2016–7/2019) were  $0.16092 \pm 0.00045$  (1  $\sigma$ ;  $n = 680$ ) and  $0.59862 \pm 0.00186$  (1  $\sigma$ ;  $n = 486$ ), respectively. Total procedural blanks during this study were  $14.3 \pm 3.9$  pg and  $0.09 \pm 0.01$  pg (1 $\sigma$  S.D.,  $n = 6$ ) for Re and Os, respectively, with an average  $^{187}\text{Os}/^{188}\text{Os}$  value of  $0.24 \pm 0.02$

( $n=6$ ). Initial osmium ratios ( $\text{Os}_i$ ) are calculated at age of 94.0 Ma for the Cenomanian–Turonian stage boundary<sup>13</sup> using the present-day measured  $^{187}\text{Re}/^{188}\text{Os}$  and  $^{187}\text{Os}/^{188}\text{Os}$  values of samples and the  $^{187}\text{Re}$  decay constant ( $\lambda = 1.666 \times 10^{-11}\text{yr}^{-1}$ )<sup>45</sup>.

**X-ray fluorescence (XRF) analysis.** About 5 g of fresh mudstone was dried at 50 °C for 24 h and ground to  $<38\text{ }\mu\text{m}$  with a Multibeads Shocker pulverizer. Pressed powder samples were determined bulk element compositions using a wavelength-dispersive XRF instrument (S8 Tiger, Bruker) at the Technical Division, School of Engineering, Tohoku University. The relative standard deviation was less than 1.5 %.

**The degree of pyritization (DOP).** The dry combustion method measured the total sulfur content using an elemental analyzer (YHS-11, Yanaco) at Tohoku University. The reactive part of Fe was extracted following the method of ref. <sup>39</sup>, by mixing 100 mg of a finely ground sample with 5 ml of 1 N HCl for 24 h. Measurements were determined with Inductively coupled plasma atomic emission spectrometry (ICPS-8100, Shimadzu) at the Hokkaido Industrial Research Institute. The DOP was calculated using the equation  $\text{DOP} = \text{Fe}_{\text{pyrite}}/(\text{Fe}_{\text{pyrite}} + \text{Fe}_{\text{reactive}})$ . Pyrite-bound Fe ( $\text{Fe}_{\text{pyrite}}$ ) was approximated by multiplying the S content by 0.871.

**Clay mineral analysis.** The clay sample used to estimate the illite crystallinity was separated from each powdered sample in the OC section by gravity sedimentation and was formed into the XRD clay cake by the filter transfer method<sup>46</sup>. X-ray diffraction (XRD) measurements were performed on a Rigaku X-ray Diffractometer RINT 2100 V, using  $\text{CuK}\alpha$  radiation monochromatized by a curved graphite crystal in the step scan method. The decomposition procedure ref. <sup>26</sup> of the obtained XRD patterns was performed with a program XRD MacDiff<sup>47</sup>. The illite crystallinity was estimated using a modified Lanson index (MLI)<sup>26</sup> determined using the decomposition data.

**Biomarker analysis.** Lipids were extracted with methanol, dichloromethane–methanol (1:1), and dichloromethane. The extract was separated into four fractions by silica gel column chromatography: F1 4 ml hexane, F2 4 ml hexane–toluene (3:1), F3 4 ml hexane–ethyl acetate (9:1), and F4 4 ml ethyl acetate–methanol (1:1). The hydrocarbon fractions (aliphatic F1 and aromatic F2) were analyzed by gas chromatography–mass spectrometry (GC-MS) using an Agilent 7890B GC coupled with an Agilent 5977 A MSD. An Agilent J&W DB-5HT column (30 m  $\times$  0.25 mm  $\times$  0.1  $\mu\text{m}$ ) was used with He as carrier gas with a flow rate of 1 ml/min. The oven temperature program was 50 °C (4 min) to 310 °C at 4 °C/min (held 20 min). Ionization energy was set to 70 eV. With the same analytical conditions, an Agilent 6890 N GC coupled with an Agilent 5975B Inert XL MSD was used for 24 of 90 samples<sup>48</sup>. Compounds were assigned using NIST14 and in-house spectral libraries, published spectra<sup>34</sup>. Peak areas were normalized to those of d62-triacontane and d50-tetracosane (F2) internal standards added before the separation and GC-MS analysis. Semi-quantification of biomarkers was performed based on the relative peak areas of *n*-alkanes ( $m/z$  57), hopanes ( $m/z$  191), steranes ( $m/z$  217), and plant-derived di- and triterpenoids (characteristic ions<sup>34</sup>).

## Data availability

The data set underlying this research is available at <https://doi.org/10.1594/PANGAEA.964200>.

Received: 1 July 2023; Accepted: 11 January 2024;

Published online: 19 February 2024

## References

1. Turgeon, S. C. & Creaser, R. A. Cretaceous oceanic anoxic event 2 was triggered by a massive magmatic episode. *Nature* **454**, 323–326 (2008).
2. Leckie, R. M., Bralower, T. J. & Cashman, R. Oceanic anoxic events and plankton evolution: biotic response to tectonic forcing during the mid-Cretaceous. *Paleoceanography* **17**, 2001PA000623 (2002).
3. Schmidtko, S., Stramma, L. & Visbeck, M. Decline in global oceanic oxygen content during the past five decades. *Nature* **542**, 335–339 (2017).
4. Kuroda, J. et al. Contemporaneous massive subaerial volcanism and late Cretaceous Oceanic Anoxic Event 2. *Earth Planet. Sci. Lett.* **256**, 211–223 (2007).
5. Percival, L. M. E., van Helmond, N. A. G. M., Selby, D., Goderis, S. & Claeys, P. Complex interactions between large igneous province emplacement and global-temperature changes during the Cenomanian–Turonian oceanic anoxic event (OAE2). *Paleoceanogr. Paleoclimatol.* **35**, e2020PA004016 (2020).
6. Gale, A. S. & Christensen, W. K. Occurrence of the belemnite *Actinocamax* plenus in the Cenomanian of SE France and its significance. *Bull. Geol. Soc. Denmark* **43**, 68–77 (1996).
7. Sullivan, D. L. et al. High-resolution osmium data record three distinct pulses of magmatic activity during the Cretaceous Oceanic Anoxic Event 2 (OAE2). *Geochim. Cosmochim. Acta* **285**, 257–273 (2020).
8. Jenkyns, H. C., Dickson, A. J., Ruhl, M. & Boorn, S. H. Basalt–seawater interaction, the Plenus Cold Event, enhanced weathering and geochemical change: deconstructing Oceanic Anoxic Event 2 (Cenomanian–Turonian, Late Cretaceous). *Sedimentology* **64**, 16–43 (2017).
9. Robinson, S. A. et al. Southern Hemisphere sea-surface temperatures during the Cenomanian–Turonian: implications for the termination of Oceanic Anoxic Event 2. *Geology* **47**, 131–134 (2019).
10. Heimhofer, U. et al. The vegetation response to exceptional global warmth during Oceanic Anoxic Event 2. *Nat. Commun.* **9**, 3832 (2018).
11. Takashima, R. et al. Prevailing oxic environments in the Pacific Ocean during the mid-Cretaceous Oceanic Anoxic Event 2. *Nat. Commun.* **2**, 234 (2011).
12. Gangl, S. K. et al. High-resolution records of Oceanic Anoxic Event 2: Insights into the timing, duration and extent of environmental perturbations from the palaeo-South Pacific Ocean. *Earth Planet. Sci. Lett.* **518**, 172–1820 (2019).
13. Jones, M. M., Sageman, B. B., Selby, D., Jicha, B. R. & Singer, B. S. Regional chronostratigraphic synthesis of the Cenomanian–Turonian oceanic anoxic event 2 (OAE2) interval, Western Interior Basin (USA): new Re–Os chronostratigraphy and  $^{40}\text{Ar}/^{39}\text{Ar}$  geochronology. *GSA Bull.* **133**, 1090–1104 (2020).
14. Takashima, R. et al. Geology and stratigraphy of forearc basin sediments in Hokkaido, Japan: cretaceous environmental events on the northwest Pacific margin. *Cret. Res.* **25**, 365–390 (2004).
15. Zhou, J., Poulsen, C. J., Rosenbloom, N., Shields, C. & Briegleb, B. Vegetation–climate interactions in the warm mid-Cretaceous. *Clim. Past* **8**, 565–576 (2012).
16. Eldrett, J. S. et al. Astronomically calibrated stratigraphy of the Cenomanian–Turonian Eagle Ford Formation, Texas, USA: implications for global chronostratigraphy. *Cret. Res.* **56**, 316–344 (2015).
17. Jones, M. M. et al. Astronomical pacing of relative sea level during Oceanic Anoxic Event 2: preliminary studies of the expanded SH#1 Core, Utah, USA. *GSA Bull.* **131**, 1702–1722 (2019).
18. Paul, C. R. C. et al. The Cenomanian–Turonian boundary at Eastbourne (Sussex, UK): a proposed European reference section. *Palaeogeogr. Palaeoclimatol. Palaeoecol.* **150**, 83–121 (1999).
19. Takashima, R. et al. Establishment of Upper Cretaceous bio- and carbon isotope stratigraphy in the northwest Pacific Ocean and radiometric ages around the Albian/Cenomanian, Coniacian/Santonian and Santonian/Campanian boundaries. *Newslett. Stratigr.* **52/3**, 341–376 (2019).
20. Elrick, M., Molina-Garza, R., Duncan, R. & Snow, L. C-isotope stratigraphy and paleoenvironmental changes across OAE2 (mid-Cretaceous) from shallow-water platform carbonates of southern Mexico. *Earth. Planet. Sci. Lett.* **277**, 295–306 (2009).
21. Du Vivier, A. D. et al. Marine  $^{187}\text{Os}/^{188}\text{Os}$  isotope stratigraphy reveals the interaction of volcanism and ocean circulation during Oceanic Anoxic Event 2. *Earth Planet. Sci. Lett.* **389**, 23–33 (2014).
22. Du Vivier, A. D. C., Selby, D., Condon, D. J., Takashima, R. & Nishi, H. Pacific  $^{187}\text{Os}/^{188}\text{Os}$  isotope and U–Pb geochronology: Synchronicity of global Os isotope change across OAE 2. *Earth Planet. Sci. Lett.* **428**, 204–216 (2015).
23. Li, Y.-X. et al. Enhanced ocean connectivity and volcanism instigated global onset of Cretaceous Oceanic Anoxic Event 2 (OAE2) ~94.5 million years ago. *Earth Planet. Sci. Lett.* **578**, 117331 (2022).

24. Jones, M. M. et al. Abrupt episode of mid-Cretaceous ocean acidification triggered by massive volcanism. *Nat. Geosci.* **16**, 169–174 (2023).

25. Lu, X., Kendall, B., Stein, H. J. & Hannah, J. L. Temporal record of osmium concentrations and  $^{187}\text{Os}/^{188}\text{Os}$  in organic-rich mudrocks: Implications for the osmium geochemical cycle and the use of osmium as a paleoceanographic tracer. *Geochim. Cosm. Acta* **216**, 221–241 (2017).

26. Lanson, B. The decomposition of experimental X-ray diffraction patterns (profile fitting): a convenient way to study clay minerals. *Clays Clay Miner.* **45**, 132–146 (1997).

27. Kuwahara, Y. et al. Controlling weathering and erosion intensity on the southern slope of the Central Himalaya by the Indian summer monsoon during the last glacial. *Global Planets Changes* **71**, 73–84 (2010).

28. Forster, A., Schouten, S., Moriya, K., Wilson, P. A. & Sissinghe Damsté, J. S. Tropical warming and intermittent cooling during the Cenomanian/Turonian oceanic anoxic event 2: Sea surface temperature records from the equatorial Atlantic. *Paleoceanography* **22**, PA1219 (2007).

29. Sissinghe Damsté, J. S., van Bentum, E. C., Reichart, G. J., Pross, J. & Schouten, S. A  $\text{CO}_2$  decrease–driven cooling and increased latitudinal temperature gradient during the mid-Cretaceous Oceanic Anoxic Event 2. *Earth Planet. Sci. Lett.* **293**, 97–103 (2010).

30. van Helmond, N. A. G. M. et al. A perturbed hydrological cycle during Oceanic Anoxic Event 2. *Geology* **42**, 123–126 (2014).

31. Gernon, T. M. et al. Global chemical weathering was dominated by continental arcs since the mid-Paleozoic. *Nat. Geosci.* **14**, 690–696 (2021).

32. Lo, F.-L., Chen, H.-F. & Fang, J.-N. Discussion of suitable chemical weathering proxies in sediments by comparing the dissolution rates of minerals in different rocks. *J. Geol.* **125**, 83–99 (2017).

33. Pogg von Strandmann, P. A. E., Jenkyns, H. C. & Woodfine, R. G. Lithium isotope evidence for enhanced weathering during Oceanic Anoxic Event 2. *Nat. Geosci.* **6**, 668–672 (2013).

34. Nakamura, H., Sawada, K. & Takahashi, M. Aliphatic and aromatic terpenoid biomarkers in Cretaceous and Paleogene angiosperm fossils from Japan. *Org. Geochem.* **41**, 975–980 (2010).

35. Killops, S. D., Raine, J. I., Woolhouse, A. D. & Weston, R. J. Chemostratigraphic evidence of higher-plant evolution in the Taranaki Basin, New Zealand. *Org. Geochem.* **23**, 429–445 (1995).

36. Wing, S. L. & Boucher, L. D. Ecological aspects of the Cretaceous flowering plant radiation. *Annu. Rev. Earth Planet. Sci.* **26**, 379–421 (1998).

37. Friis, E. M., Crane, P. R. & Pedersen, K. R. *Early Flowers and Angiosperm Evolution* (Cambridge University Press, 2011).

38. Birks, H. J. B. Angiosperms versus gymnosperms in the Cretaceous. *PNAS* **117**, 30879–30881 (2020).

39. Raiswell, R., Buckley, F., Berner, R. A. & Anderson, T. F. The degree of pyritization of iron as a paleoenvironmental indicator of bottom-water oxygenation. *J. Sediment. Petr.* **58**, 812–819 (1988).

40. Ostrander, C. M., Owens, J. D. & Nielsen, S. G. Constraining the rate of oceanic deoxygenation leading up to a Cretaceous Oceanic Anoxic Event (OAE-2: ~94 Ma). *Sci. Adv.* **3**, e1701020 (2017).

41. Ozaki, K., Tajima, S. & Tajika, E. Conditions required for oceanic anoxia/euxinia: constraints from a one-dimensional ocean biogeochemical cycle model. *Earth Planet. Sci. Lett.* **304**, 270–279 (2011).

42. Monteiro, F. M., Pancost, R. D., Ridgwell, A. & Donnadieu, Y. Nutrients as the dominant control on the spread of anoxia and euxinia across the Cenomanian–Turonian oceanic anoxic event (OAE2): model-data comparison. *Paleoceanography* **27**, PA4209 (2012).

43. Scotese, C. R. *Atlas of Late Cretaceous Maps, PALEOMAP Atlas for ArcGIS* Volume 2, The Cretaceous, Maps 16–22, Mollweide Projection, (PALEOMAP Project, 2014).

44. Selby, D. & Creaser, R. A. Re–Os geochronology of organic rich sediments: an evaluation of organic matter analysis methods. *Chem. Geol.* **200**, 225–240 (2003).

45. Smoliar, M. I., Walker, R. J. & Morgan, J. W. Re–Os ages of group IIA, IIIA, IVA, and IVB iron meteorites. *Science* **271**, 1099–1102 (1996).

46. Moore, D. M. & Reynolds Jr, R. C. *X-ray Diffraction and the Identification and Analysis of Clay Minerals* 332 (Oxford University Press, 1989).

47. Petschick, R. *MacDiff Ver. 4.2.3, Manual. Geologisch-Paläontologisches Institut Johann Wolfgang-Universität Frankfurt am Main Senckenberganlage 58* (Frankfurt am Main, 2000).

48. Ando, T. et al. Depositional environments and maturity were evaluated by biomarker analyses of sediments deposited across the Cenomanian–Turonian boundary in the Yezo Group, Tomamae area, Hokkaido, Japan. *Island Arc.* **26**, e12178 (2017).

## Acknowledgements

We express our appreciation to K. Omatsu, S. Moribe, and S. Kuwabara, for their help with fieldwork. Chris Ottley and Geoff Nowell are acknowledged for their laboratory support. This study was carried out with the support of KAKENHI (21H04503 and 18KK0091) to R.T., (20H02012) to H.N.

## Author contributions

Study conceptualization was performed by R.T., D.S. and H.N. Geochemical analyses were performed by D.S., Y.K., R.T., M.N. and M.U. Organic geochemical analyses were by T.Y., H.N., K.S., M.I., and T.K. Microfossil analyses by H.N., A.K. and R.G.B. All authors contributed to manuscript editing.

## Competing interests

The authors declare no competing interests.

## Additional information

**Supplementary information** The online version contains supplementary material available at <https://doi.org/10.1038/s43247-024-01214-z>.

**Correspondence** and requests for materials should be addressed to R. Takashima.

**Peer review information** *Communications Earth & Environment* thanks Richard Ernst and the other, anonymous, reviewer(s) for their contribution to the peer review of this work. Primary Handling Editors: Mojtaba Fakhraee, Joe Aslin, Aliénor Lavergne and Carolina Ortiz Guerrero. Peer reviewer reports are available.

**Reprints and permission information** is available at <http://www.nature.com/reprints>

**Publisher's note** Springer Nature remains neutral with regard to jurisdictional claims in published maps and institutional affiliations.



**Open Access** This article is licensed under a Creative Commons Attribution 4.0 International License, which permits use, sharing, adaptation, distribution and reproduction in any medium or format, as long as you give appropriate credit to the original author(s) and the source, provide a link to the Creative Commons license, and indicate if changes were made. The images or other third party material in this article are included in the article's Creative Commons license, unless indicated otherwise in a credit line to the material. If material is not included in the article's Creative Commons license and your intended use is not permitted by statutory regulation or exceeds the permitted use, you will need to obtain permission directly from the copyright holder. To view a copy of this license, visit <http://creativecommons.org/licenses/by/4.0/>.

© The Author(s) 2024